Heat and Mass Transfer in Water-Laden Sandstone: Convective Heating

CHEN KOU WEI and
H. T. DAVIS

Department of Chemical Engineering and
Materials Science
University of Minnesota
Minneapolis, MN 55455

and

E. A. DAVIS and
JOAN GORDON

Department of Food Science and Nutrition
University of Minnesota
St. Paul, MN 55108

A theoretical model was developed to predict the heat and mass transfer phenomena in porous materials. A water-filled sandstone was heated in a convective oven and its water loss rates and temperature profiles were compared with theoretical results. In addition to local temperatures, moisture content, gas densities and pressure, this model also predicts the fluid flow pattern in the heated sample.

SCOPE

Heat and mass transfer in porous media occurs in many contemporary engineering applications, for instance, enhancing oil recovery, preparation of solid catalysts, and food processing. A familiar example in chemical engineering is drying which is normally confined to mild heating conditions. Classical explanations of interior drying phenomena are largely based on temperature history and drying-rate curves. Recently, Harmathy (1969) and Huang et al. (1979) predicted temperature, moisture content, and pressure profiles in the pendular state by different theoretical approaches, but these are not sufficient to explain the dynamic phenomena occurring in heated materials. To describe the dynamic phenomena quantitatively, we modify Whitaker's (1977) derivations and apply the new model to a sandstone subjected to mild heating conditions.

CONCLUSIONS AND SIGNIFICANCE

The predicted phenomena are shown in Figures 15–17. Temperatures in the porous medium steadily increase with time. Moisture profiles are smooth and there is no sharp front dividing dry region and wet region in this case. Water vapor densities steadily increase with time. Except for the initial perturbation caused by air equilibration, air densities steadily decrease with time. Internal gas pressure declines at the beginning and then recovers to nearly atmospheric pressure. Although there exist transient flow patterns initially, during most of the heating period water vapor condenses along its path as it flows toward the centerline of the sample; air moves in the same direction, but at smaller flux. Liquid water, however, migrates toward the surface with a flux 2 to 3 orders of magnitude larger than vapor flux.

The results obtained in this work help in understanding the pore-level heat and mass transfer phenomena. The model has potential applications in several engineering areas.

INTRODUCTION

Heat and mass transfer in porous media is an important subject in many engineering-related fields and plays a role in practical processes ranging from enhancing oil recovery and drying soils to the cooking and dehydration of food products. As a first step to understanding complex porous media, one needs to carefully evaluate and understand fluid flow in rigid porous media. Classical

explanations of interior drying phenomena are largely based on temperature and drying-rate curves. Most theoretical investigations of drying phenomena can be classified as diffusion theory (Sherwood, 1931), capillary flow theory (Ceaglske and Hougen, 1937), evaporation-condensation theory (Gurr, 1952), and the less mechanistic irreversible thermodynamic models (Lykov and Mykhaylov, 1961). Recently, Harmathy (1969) and Huang et al. (1979) predicted temperature, moisture content, and pressure profiles in the pendular state by different theoretical approaches. These are not sufficient to explain the dynamic phenomena occurring in heated materials. A convenient starting point of drying theory is the careful, recent work of Whitaker (1977), who has derived appropriate locally volume-averaged conservation equations for two-phase capillary flow in porous media.

In this study we investigate experimentally the temperature profiles and water loss rates of convectively heated water-filled nondeformable, nonreactive porous media and describe the results theoretically on the basis of conservation equations supplemented by a generalized Darcy's law, relative permeability of liquid and gas phases (Collins, 1961). The predictions of the model, which are consistent with our experimental data, help explain the mechanisms of fluid movement and temperature distributions in heated porous media.

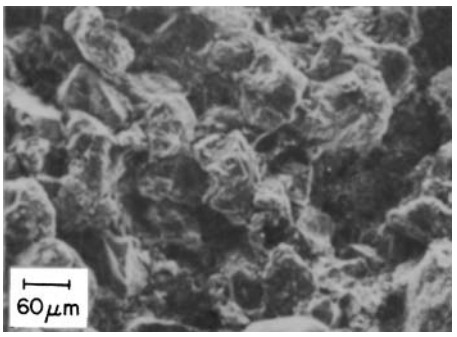

Figure 1a. SEM overview of the sandstone.

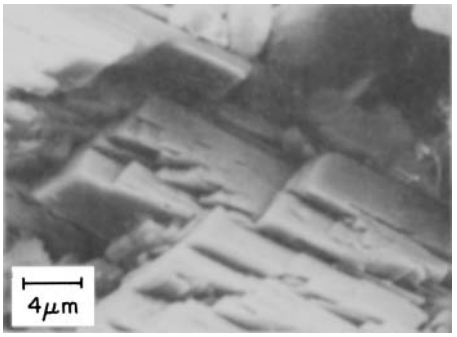

Figure 1b. Region with elemental analysis Si:Al:K ratio of 3:1:1.

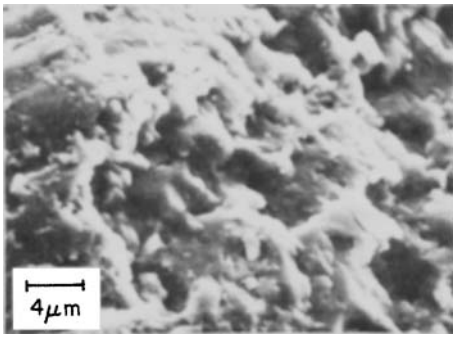

Figure 1c. Region with elemental analysis mainly Si.

EXPERIMENTAL METHODS

Sample Preparation

The sandstone sample studied is a cylinder 17.4 cm long and 5.0 cm in diameter. For theoretical considerations this approximates an infinite cylinder since the length:diameter ratio is more than 3:1. It is a water-wet (spontaneously imbibes water in the presence of air), consolidated sandstone containing clays whose composition is mainly silicate:aluminate:potassium or mainly silicates with traces of other elements such as Mg, Fe, and Ti. Figure 1a shows an SEM overview of the sandstone in terms of its three-dimensional appearance, Figure 1b shows a higher magnification area of a region whose elemental analysis by EDAX showed Si:Al:K ratios of 3:1:1 (evidence of the presence of clays), and Figure 1c shows a higher magnification area of the rock whose elemental analysis by EDAX showed mainly Si present.

Two longitudinal holes were drilled halfway through the cylinder at $\frac{1}{3}$ and $\frac{2}{3}$ of the radius from the center line for accommodating copper-constantan thermocouples made of 24-gauge wires. To fill the sandstone with water it was first dried in a conventional laboratory oven at 423.15 K, next placed in a vacuum desiccator above a water reservoir and the desiccator evacuated under 71 cm Hg vacuum for 20 min to remove air and then immersed in the water reservoir and left there for 24 h under the 71 cm Hg vacuum.

Sample characterization

1. Porosity. The porosity of the sample was found by filling a previously dried-out, evacuated system with water at room temperature (298 K; 77°F), weighing it, and drying it in the conventional oven at 423.15 K until it ceased to change weight. The porosity ϕ was computed from the formula

$$\phi = \frac{\text{(Weight of water-filled sample)} - \text{(Weight of dry sample)}}{\text{(Volume of sample at 298.15 K) (Density of water at 298.15 K)}} \quad (1)$$

The porosity was found to be $\phi = 0.22$.

2. Capillary Pressure-Saturation Curve. The capillary pressure vs. liquid water saturation (defined as the fraction of pore space filled with liquid water) was determined in the presence of air by the constant-speed centrifuge method (Hoffman, 1963). A fully saturated sandstone sample,

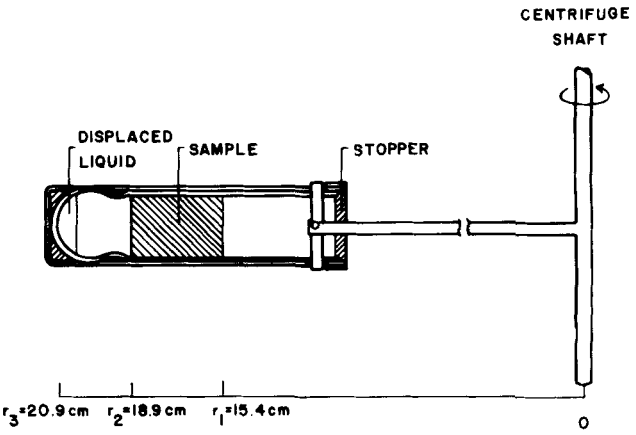

Figure 2. Diagram of cell for determining capillary pressure by centrifuge method.

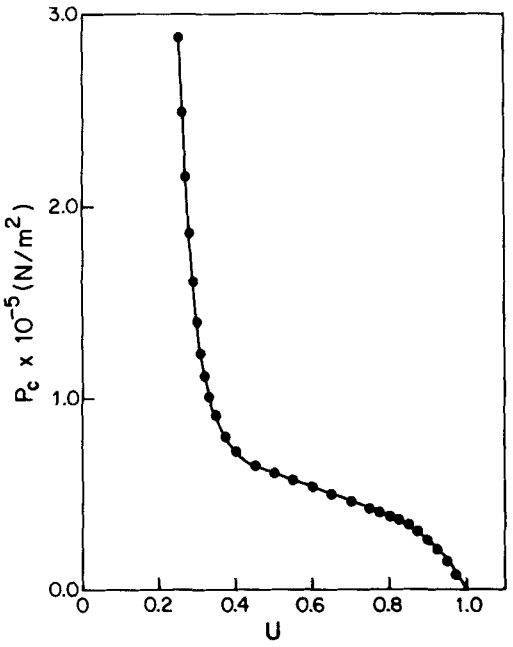

Figure 3. Capillary pressure vs. moisture saturation.

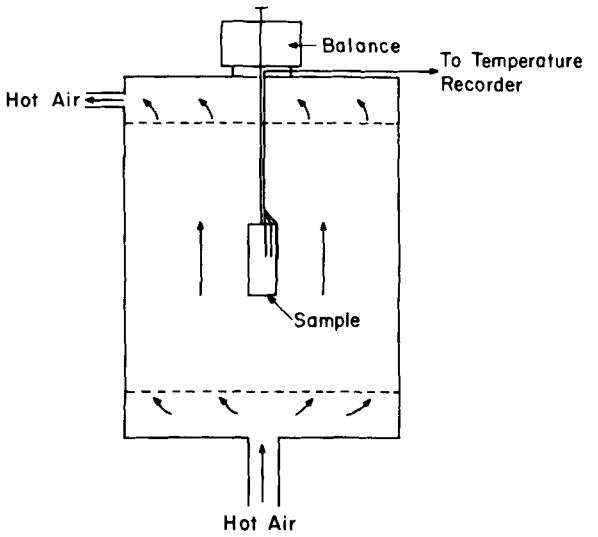

Figure 5. Diagram of the heating system.

3.4 cm long and 2.3 cm in diameter, was centrifuged in a model UV International Centrifuge until constant weight was attained, then the final weight of the sample was recorded. The experimental cell is sketched in Figure 2. Similar experiments were conducted at various rotation speeds in order to span the entire range of water saturation of the sandstone. Then the following equations were used to calculate capillary pressure P_c and moisture saturation U at the surface closer to the centrifuge's axis:

$$P_c|_{r_1} = \frac{1}{2}(\rho_l - \rho_a)\omega^2(r_2^2 - r_1^2) \tag{2}$$

$$U|_{r_1} = \frac{2r_1}{r_1 + r_2}\left(\overline{U} + \frac{\omega}{2}\frac{d\overline{U}}{d\omega}\right) \tag{3}$$

where ρ_l and ρ_a are the liquid water and air densities, respectively; ω the angular velocity of the centrifuge; and r_1 and r_2 the radial distances of the inner and outer sample surfaces from the axis of the centrifuge. $\overline{U}$ is the average water saturation of the sample and is defined as

$$\overline{U} \equiv \frac{\text{(Final weight of sample)} - \text{(Weight of dry sample)}}{\text{(Initial weight of sample)} - \text{(Weight of dry sample)}}$$

Liquid saturation represents the fraction of pore space filled with liquid.

The capillary pressure vs. saturation is plotted in Figure 3. This is the so-called drainage capillary pressure curve (Collins, 1961), i.e., the capillary pressure arrived at in an experimental sequence in which the saturation of the wetting phase (water) decreases. This is the curve relevant to the drying phenomena of interest here.

3. *One-Phase Permeability.* The permeability of the sandstone was determined with the Penn State method (Morse, 1947), using liquid water as the fluid. A sandstone sample (9.8 cm long and 4.9 cm in diameter) was mounted in a permeability cell as shown in Figure 4. Water was pumped at constant flow rate with a high-pressure liquid chromatography pump, model 6000A from Water Associates, Milford, Mass. The pressure across the sample section was measured with a pressure transducer when the system reached steady state. The permeability, K, was calculated from Darcy's law:

$$K = \frac{\text{(Viscosity of water)(Volumetric flow rate)(Length of sample)}}{\text{(Pressure drop)(Cross-sectional area of sample)}} \tag{4}$$

The value obtained K = 0.018 Darcy = 1.779×10^{-10} $(\mu m)^2$, which is comparable with the permeability of Woodbine sandstone of the same porosity (Collins, 1961).

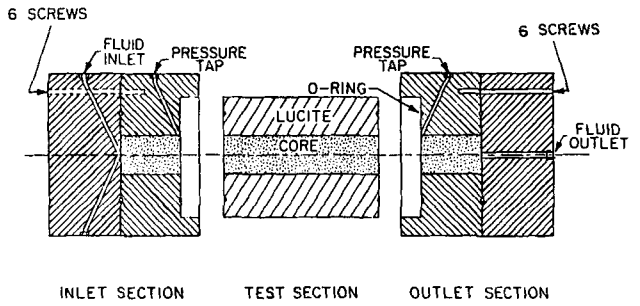

Figure 4. Permeability measurement cell (Pathak, 1981).

Drying Experiments

The heating system, with the layout shown in Figure 5, is a specially constructed oven with controllable heating elements and air flow rate. The oven is described elsewhere (Hung, 1980). For receiving the water-filled sample with mounted thermocouples, the oven was heated to 394 K (250°F) with flow rate set at 0.245 m/s. Prior to the sandstone's being suspended at the center of the oven, Teflon discs were used to cover the ends of the cylindrical sample. After the door was secured, temperatures were continuously monitored by a multichannel chart recorder, and weight loss was measured with a balance every 4 min for a period of 1 h. Also, the fraction of wet surface was estimated by dividing the darker area (wet surface) by the exposed sample surface area throughout the experiment.

THEORY

In analyzing the experimental results reported below we shall assume that the porous medium is rigid, that no chemical reactions occur in the sample, and that local thermal equilibrium exists in the porous system. One can then derive the following Darcy-level conservation equations (Whitaker, 1977). "Darcy-level " means local quantities averaged over a volume small on the macroscopic scale but large on the scale of an individual pore.

Thermal Energy Equation

$$\rho C_p \frac{\partial T}{\partial t} + (\rho_l C_{pl} \bar{v}_l + \rho_g C_{pg} \bar{v}_g) \cdot \nabla T + \Delta h_{vap} \dot{m} = \nabla \cdot (\kappa_{eff} \cdot \nabla T) \quad (5)$$

in which ρC_p is the volume-averaged heat capacity per unit volume of sample; T the local temperature; t the time; C_{pl} and C_{pg} the liquid and gas specific heat, respectively; $\bar{v}_l$ and $\bar{v}_g$ the Darcy-level superficial velocities; ρ_g the gas density; Δh_{vap} the heat of vaporization per unit mass; m the mass rate of vaporization per unit volume; and κ_{eff} the total effective thermal conductivity tensor.

Liquid Phase Continuity Equation

$$\frac{\partial(\epsilon_l \rho_l)}{\partial t} + \nabla \cdot (\rho_l \bar{v}_l) + \dot{m} = 0 \quad (6)$$

where ϵ_l is the liquid volume fraction.

Gas Phase Continuity Equation

$$\frac{\partial}{\partial t}(\epsilon_g \rho_g) + \nabla \cdot (\rho_g \bar{v}_g) = \dot{m} \quad (7)$$

where ϵ_g is the gas volume fraction.

Gas Phase Diffusion Equation

$$\frac{\partial}{\partial t}(\epsilon_g \rho_a) + \nabla \cdot (\rho_a \bar{v}_g) = \nabla \cdot [\rho_g \boldsymbol{D}_{eff,a} \cdot \nabla(\rho_a / \rho_g)] \quad (8)$$

where $\boldsymbol{D}_{eff,a}$ is the effective diffusion tensor of air in the air-water vapor mixture. Although the formulas given in this section are valid for anisotropic porous media, we use only their isotropic limits in the analysis given below.

Liquid in a drying porous medium exists in either isolated or accessible states, i.e, in discrete patches surrounded by vapor or in sample-spanning regions accessible from the surface of the sample. Accessible liquid can deliver moisture to the sample surface by liquid convection, a process much more effective for moisture release than vaporization followed by gaseous diffusion and convection, the process whereby isolated liquid can deliver moisture to the surface.

According to percolation theory (Kirkpatrick, 1973; Larson et al., 1981; Heiba et al., 1982), below a critical liquid volume fraction, ϵ_c, the percolation threshold, all liquid in the porous medium will be isolated. Above ϵ_c the accessible fraction of liquid increases monotonically toward the liquid volume fraction ϵ_l as ϵ_l increases. As the percolation threshold is approached in drainage—i.e., in a process in which wetting fluid (water) is displaced by invasion of the nonwetting fluid (air) as in the method used to measure capillary pressure—the capillary pressure begins to increase without bound (Figure 3). The permeability of the wetting phase ($\boldsymbol{K}_l$) approaches zero as the percolation threshold is approached since there it becomes hydraulically disconnected.

When the liquid phase is hydraulically connected its superficial mass average velocity obeys Darcy's law

$$\bar{v}_l = -\boldsymbol{K}_l / \mu_l \cdot [\nabla P_g + k_\epsilon \nabla \epsilon_l + k_T \nabla T - \rho_l g] \quad (9)$$

in which $k_\epsilon = -\partial P_c(\epsilon_l, T)/\partial \epsilon_l$ and $k_T = -\partial P_c(\epsilon_l, T)/\partial T$; the temperature-dependence of P_c will be estimated from $P_c = P_c(T_r) \cdot (T_c - T)/(T_c - T_r)$ where $P_c(T_r)$ represents the capillary pressure at room temperature T_r. Also, in Eq. 9, $\boldsymbol{K}_l$ and μ_l denote the permeability tensor and the liquid viscosity, respectively, and P_g the gas pressure.

In the gas phase the appropriate version of Darcy's law is

$$\bar{v}_g = -\boldsymbol{K}_g / \mu_g \cdot [\nabla P_g - \rho_g g] \quad (10)$$

where $\boldsymbol{K}_g$ and μ_g are the permeability tensor and the gas viscosity, respectively.

Kelvin's equation can be used to calculate the density of water vapor (Collins, 1961) in the temperature and pressure range of interest herein (where water vapor and air behave as ideal gas):

$$\rho_v = \rho_{v,satd} \exp(-P_c \tilde{V}_l / R_g T) \quad (11)$$

where ρ_v is the water vapor density and $\rho_{v,satd}$ represents the saturated water vapor density at temperature T; and $\tilde{V}_l$ and R_g the liquid molar volume and gas constant, respectively.

The initial conditions appropriate for the experiment considered are

$$\epsilon_l(t = 0, r) = \epsilon_{li}, P_g(t = 0, r) = P_{atm}, \text{ and } T(t = 0, r) = T_i. \quad (12)$$

Besides the symmetry condition applied at the center of the sample, three surface boundary conditions are imposed. The first is the thermal condition:

$$h(T_e - T)\boldsymbol{n} = \kappa_{eff} \cdot \nabla T + \Delta h_{vap} A_{eff} M_w N_{vs} \quad (13)$$

where T_e is the ambient temperature; $\boldsymbol{n}$ the unit outer normal vector to the sample's surface; A_{eff} the fraction of wet surface; and

TABLE I. PHYSICAL PROPERTIES AND CONSTANTS FOR THE DRYING MODEL

Symbol	Value or Expression	Unit	Reference*
C_{pa}	1,025.766	J/kg·K	a
C_{pl}	4,216.108	J/kg·K	a
C_{ps}	816.426	J/kg·K	a
C_{pv}	1842.192	J/kg·K	a
$D_{eff,a}$	$2.83 \times 10^{-5} \epsilon_g$	m^2/s	—
Δh_{vap}	Taken from steam tables	—	b
κ_g	2.699×10^{-2}	W/m·K	a
κ_l	0.653	W/m·K	a
κ_s	1.852	W/m·K	c
κ_{eff}	$\epsilon_s \kappa_s + \epsilon_l \kappa_l + \epsilon_g \kappa_g$	W/m·K	—
K	1.779×10^{-10}	$(\mu m)^2$	This work
M_a	2.897×10^{-2}	kg/mol	d
M_w	1.8015×10^{-2}	kg/mol	d
R	2.5	cm	—
R_g	8.31431	J/mol·K	d
T_c	647.3	K	e
T_e	394.26	K	—
Ti	294.26	K	—
ϵ_c	0.048	—	—
ϕ	0.22	—	—
ϵ_s	0.78	—	—
μ_g	1.7×10^{-5}	kg/m·s	d
μ_l	$\mu_l(T)$	kg/m·s	e
ρ_l	$\rho_l(T)$	kg/m^2	e
ρ_s	2.7182×10^3	kg/m^3	This work
$\rho_{v,satd}$	$\rho_{v,satd}(T)$	kg/m^3	b
h	20.92	$W/m^2 \cdot K$	a
k_x	0.2	$mol/m^2 \cdot s$	a
W	0.245	m/s	This work
ρ_{ae}	0.88	kg/m^3	a
ρ_{ve}	0.01	kg/m^3	a

* Reference: a, Perry and Chilton (1973); b, ASME (1967); c, Myers (1971); d, Bird et al. (1960); e, Weast and Astle (1982).

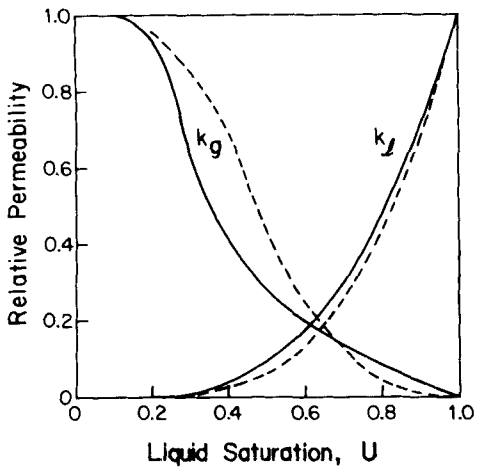

Figure 6. Relative permeability curves. — adapted from sandstone data (Scheidegger, 1972); - - - from theory (Heiba et al., 1982).

M_w the molecular weight of water. The second surface boundary condition is for liquid moisture:

$$\rho_l \bar{v}_l = A_{\text{eff}} M_w N_{vs} - \rho_v \bar{v}_g - \rho_g D_{\text{eff},a} \cdot \nabla(\rho_a/\rho_g) \quad (14)$$

The third boundary condition is that the gas pressure at the surface is chosen as 1 atm (101 kPa).

SOURCES OF PHYSICAL PROPERTIES

To make theoretical predictions a large collection of physical properties must be known. Many of these can be taken from the literature and are presented in Table 1.

The capillary pressure (Figure 3) and permeability K were measured in this work. From the limiting value of liquid saturation reached by increasing P_c, the percolation threshold ϵ_c was estimated to be 0.048. Since the porous material is assumed to be isotropic, the liquid and gas permeabilities, K_l and K_g, are related to the permeability K and the relative permeabilities of the liquid and gas phases, k_l and k_g, by the relationships $K_l = Kk_l$ and $K_g = Kk_g$. Relative permeabilities are functions of liquid saturation for a given porous medium and in slow flow (Heiba et al., 1982). For the present work, relative permeability curves given by Scheidegger (1972) were modified to have the drainage features and liquid percolation threshold of the sandstone (Figure 6, solid curves). Alternatively, purely theoretical relative permeability curves for water-wet sandstone having a residual water saturation of ϵ_c = 0.048 could be used. A. Heiba (private communication) generated

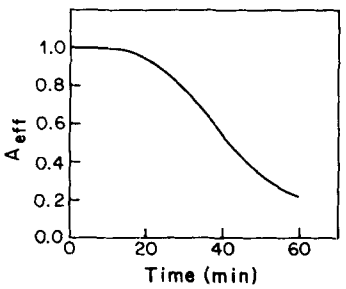

Figure 7. Fraction of wet surface area vs. time.

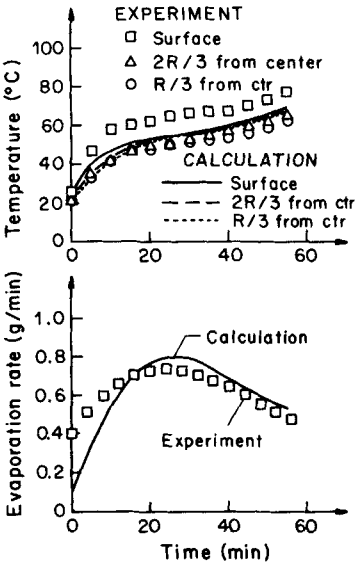

Figure 8. Histograms of temperature profile and evaporation rate for sandstone.

such curves (Figure 6, dashed curves) using the theory of Heiba et al. (1982). The numerical results obtained with the solid and dashed curves in Figure 6 differ very little and so the solid ones were used. In Figure 6, the amount of liquid is expressed in saturation $U \equiv \epsilon_l/\phi$.

The total thermal conductivity κ_{eff} of the fluid-filled porous medium was estimated from the formula $\kappa_{\text{eff}} = \epsilon_s\kappa_s + \epsilon_l\kappa_l + \epsilon_g\kappa_g$, ϵ_i and κ_i being the volume fraction and thermal conductivity of phase i. Since the solid and liquid thermal conductivities are similar in magnitude and much larger than that of the vapor, a more sophisticated model (e.g., Jefferson et al., 1958, or Mohanty et al., 1982) is not deemed necessary. ρC_p was calculated from the formula $\epsilon_s\rho_s C_{ps} + \epsilon_l\rho_l C_{pl} + \epsilon_g\rho_g C_{pg}$. Since the gas diffusion coefficient is not a strong function of temperature and in this study spatial temperature variation within the sample is small, we assume the total effective diffusivity is temperature-independent. Also,

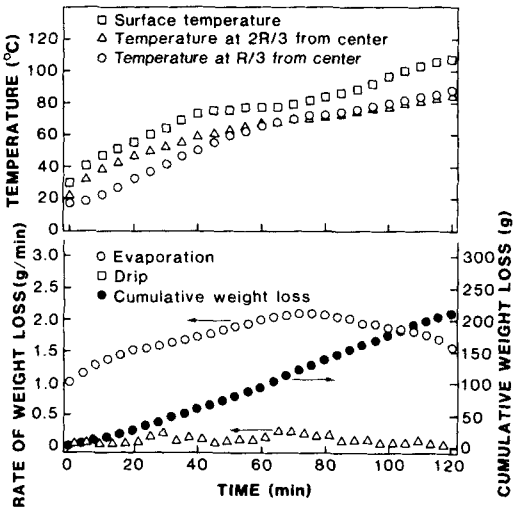

Figure 9. Histograms of temperature profile and evaporation rate for bovine muscle heated at 350°F (176.7°C).

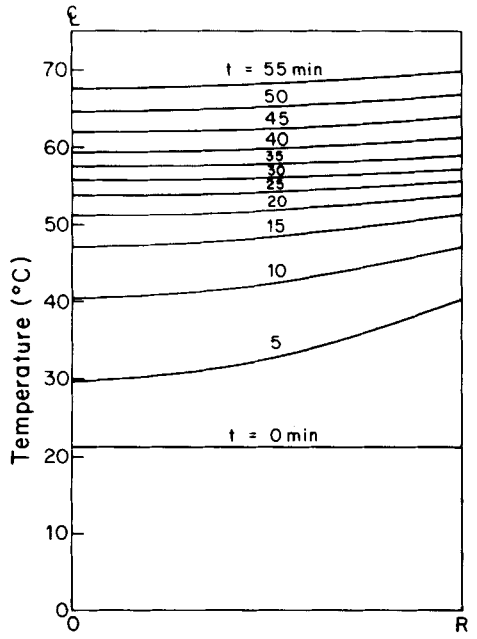

Figure 10. History of temperature profile.

Whitaker (1977) suggested that the total effective diffusivity is a linear function of ϵ_g, if dispersion is negligible. Thus, we assume that $D_{\text{eff},a} = 2.83 \times 10^{-5}\ \epsilon_g$ m^2/s. The heat and mass transfer coefficients, h and k_x, were estimated from limited drying data. We estimated k_x from film theory (Bird et al., 1960), according to which

$$1 + \frac{x_{ws} - x_{w\infty}}{\dfrac{N_{ws}}{N_{ws} + N_{as}} - x_{ws}} = \left(\frac{N_{ws} + N_{as}}{k_x}\right)$$

where x_{ws} and $x_{w\infty}$ are the mole fraction of water vapor at the wet sample surface and in the drying medium, and N_{ws} and N_{as} are

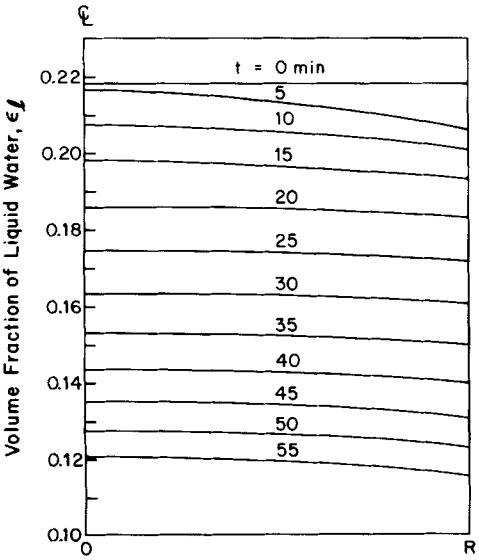

Figure 11. History of liquid saturation distribution.

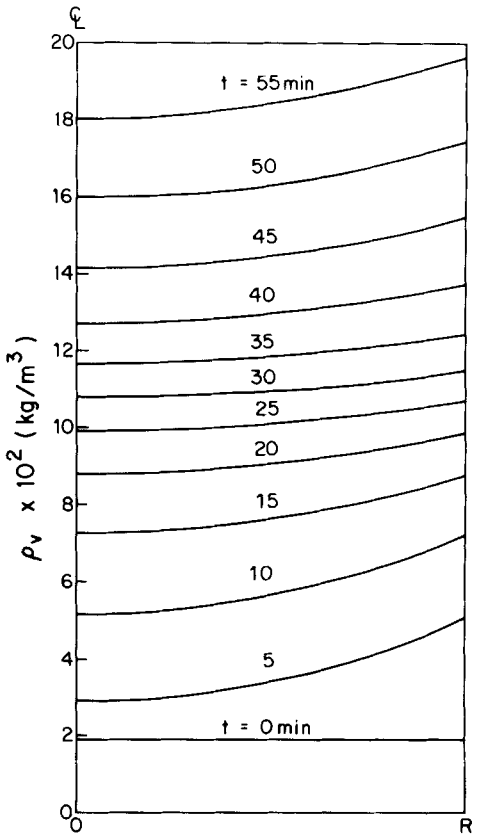

Figure 12. History of vapor density profile.

the flux of water vapor and air at the sample surface. For the experiments reported here air flux was negligible. The flux of water vapor was calculated as the rate of water lost by the sample divided by the wet surface area of the sample. Using data taken at 20 min, we estimated $k_x = 0.2$ mol/m^2·s. The heat transfer coefficient, h, was estimated from the thermal boundary condition, Eq. 13, with data also taken at 20 min. The calculated value of heat transfer coefficient was $h = 20.92$ W/m^2·K.

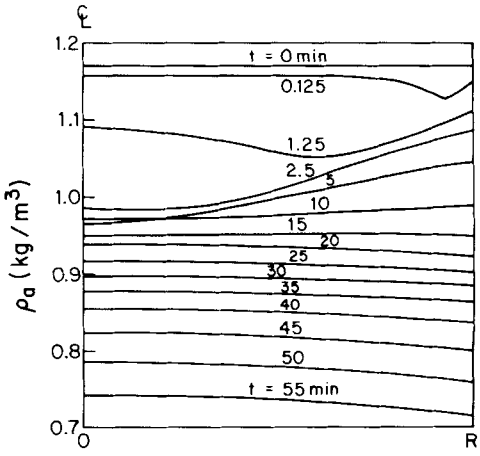

Figure 13. History of air density profile.

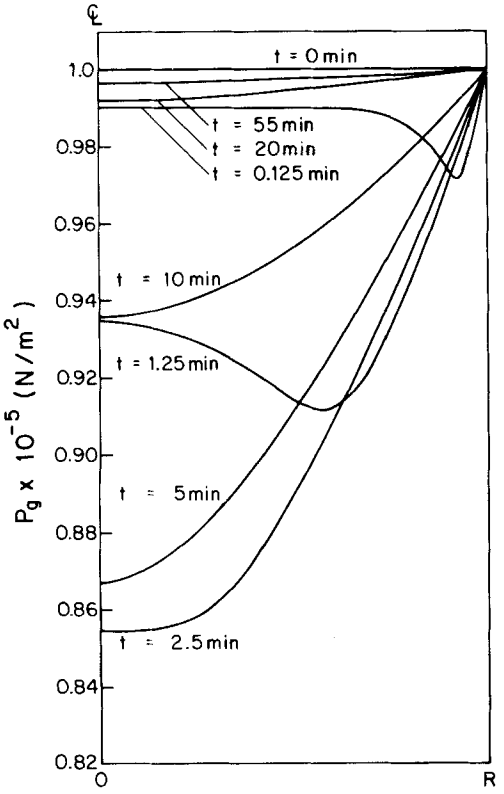

Figure 14. History of gas pressure distribution.

NUMERICAL ANALYSIS

A one-dimensional model is employed in the analysis since the sample approximates an infinite cylinder with both ends insulated. Physical properties discussed in the last section were used in the calculations.

To facilitate the numerical solutions of these nonlinear equations, the following dimensionless variables are introduced:

$$\theta \equiv \frac{T - T_e}{T_i - T_e} \tag{15}$$

$$U \equiv \frac{\epsilon_l}{\epsilon_{l_i}} \tag{16}$$

$$V^{(1)} \equiv \frac{\rho_v - \rho_{ve}}{\rho_{v_i} - \rho_{ve}} \tag{17}$$

$$V^{(2)} \equiv \frac{\rho_a}{\rho_{ae}} \tag{18}$$

$$x \equiv r/R \tag{19}$$

and

$$\tau \equiv \alpha_s t/R^2 \tag{20}$$

where the subscript e refers to the oven condition, the subscript i refers to the initial condition, and $\alpha_s = k_s/\rho_s C_{ps}$ is the solid thermal diffusivity. After Eqs. 5–14 were nondimensionalized, they were discretized. The discretized equations we used are found in the Appendix. These equations were then solved by a three-point, two-level implicit finite difference method. Briefly, on each grid the spatial derivatives were approximated by central difference expressions at a new time level and their coefficients were evaluated with the variables of the previous time level. The time differentiation was replaced by the difference form over new and previous time levels. Having combined with the boundary conditions, the algebraic equations could be put in the compact form $\boldsymbol{Ax} = \boldsymbol{b}$ where the matrix A was tridiagonal. Then, the Gauss elimination method was employed to solve for the variable x at a new time level. This procedure was carried out repeatedly moving along the time axis. The solutions turned out to be smooth. To test this accuracy, we also solved the problem with an orthogonal collocation method (Villadsen and Stewart, 1967), which often works better than other schemes for problems without a sharp front. The two sets of solutions agree and are discussed in the next section.

RESULTS AND DISCUSSION

From the theoretical model and experimental information from this study as well as previous studies from our laboratory, the following information emerges. During the heating process the surface of the sandstone was completely wet in the first 12 min; thereafter dry spots begin to appear. Thus, the specific effective area for evaporation decreases gradually. This is characterized by the results shown in Figure 7. In Figure 8 experimental water loss rate and temperature data collected for sandstone have been plotted and are compared to predictions of the theoretical model.

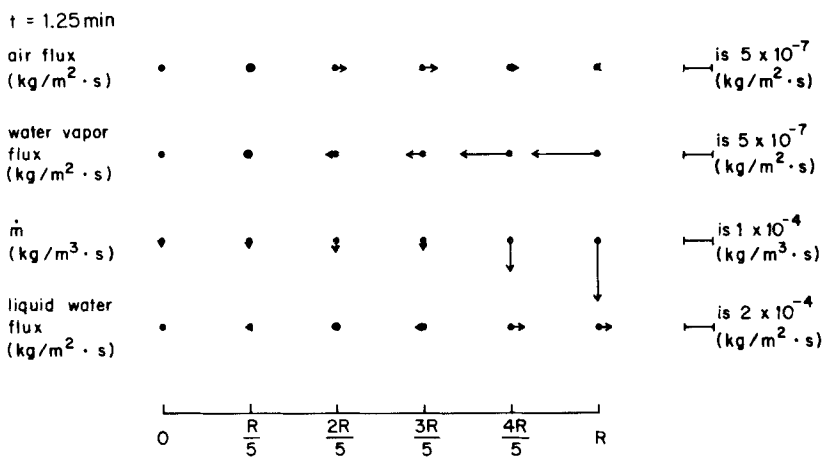

Figure 15. Predicted fluid flow pattern at 1.25 min.

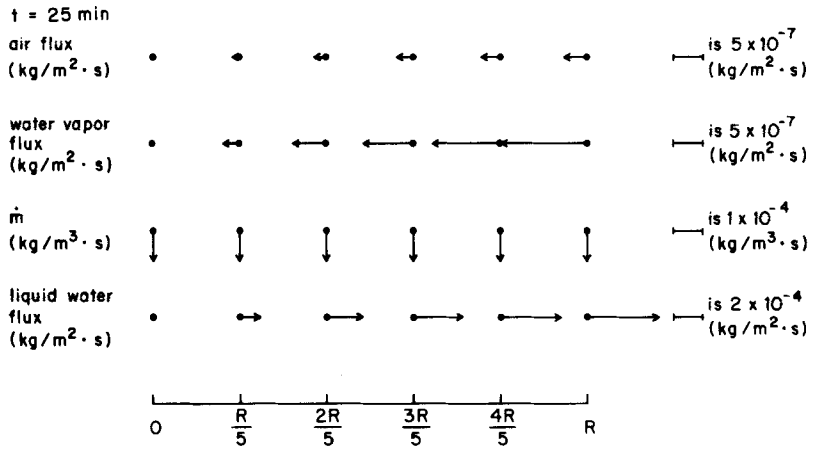

Figure 16. Predicted fluid flow pattern at 25 min.

One can see from the temperature profiles that except for the surface temperature, the experimental and theoretical curves agree quite well. The surface temperature for the experimental values were very difficult to obtain, since near the surface the temperature gradient in the drying medium is large, about 75 K/cm. Although the mechanisms of fluid flow in porous materials with fibrous structure may include diffusion as well as capillary flow, one can see from Figure 9, which shows characteristic curves for bovine muscle (Wei et al., 1981), that the sandstone and bovine muscle data are similar even though the oven temperature used is higher. Hence as a first approximation for meat fiber matrices, Darcy flow in continuous pores accounts for most of the water transport in the saturation regime examined herein (we do not consider water transport after the water saturation drops below the percolation threshold, i.e., when only isolated water exists in the sample).

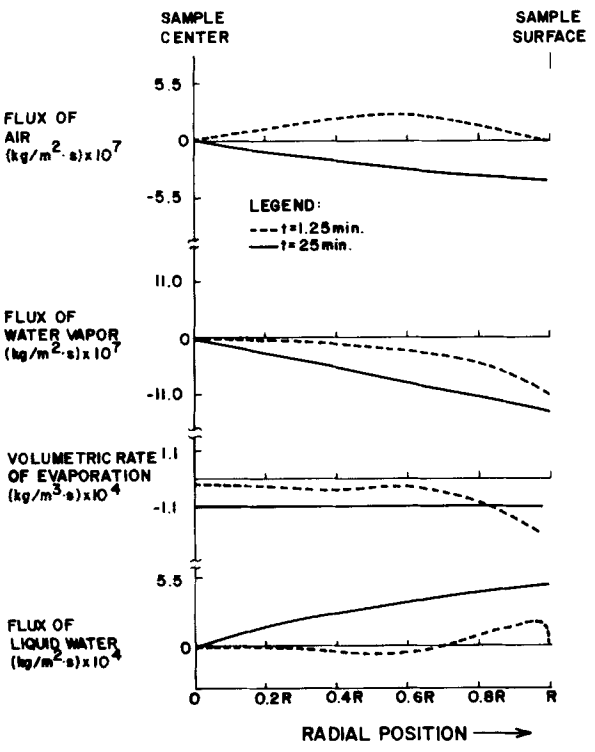

Figure 17. Profiles of predicted fluid fluxes at 1.25 and 25 min.

In Figures 10–14 are the predicted distributions of temperature, liquid content, vapor density, air density and gas pressure within the cylindrical sandstone at selected time levels. The predicted temperatures (Figure 10) in the cylinder rise rapidly in the beginning, slow down in the middle, and increase again moderately by the end of the heating period. This is due to steady decrease of convective heating caused by the increase of surface temperature and the characteristic of surface evaporation, which carried latent heat away from the sample.

Figure 11 shows the predicted history of liquid moisture distribution. That liquid saturation continuously decreased toward the surface and steadily declines with time is similar to the experimental results with unglazed pottery in the work of Toei and Okazaki (1970). Also, Peck et al. (1977) found analogous moisture profiles in fire-resistant brick. Since water may spread on the surface, the specific effective area for mass transfer, shown in Figure 7, is larger than the liquid saturation in the surface pores.

The vapor density profiles and the air density profiles at several time levels are depicted in Figures 12 and 13, respectively. Due to thermal equilibrium, the steady increase of vapor density is closely related to the temperature increase. On the other hand, valleylike shapes are found in early air density profiles which may be caused by the cool air in the cylinder diffusing toward the hot air around the sample and the resultant reversing convective air flow. After the perturbation is smoothed out, air density gradually decreases due to increase of void volume and lack of air supply.

The pressure distribution history in the gas phase within the cylinder is shown in Figure 14. The pressure valley becomes deeper and gradually loses its shape as it moves toward the centerline and after about 2.5 min heating the pressure starts to rise again.

The fluid flow patterns in the sandstone at 1.25 and 25 min are shown diagramatically in Figures 15 and 16, respectively. Although there exist transient flow patterns in the beginning, during most of the heating period water vapor condenses along its path as it flows toward the centerline. Air also moves in the same direction but at smaller flux, whereas liquid water migrates towards the surface with flux 2 to 3 orders higher than vapor flux. Detailed calculations show the convective vapor flow is enhanced by vapor diffusion, but convective air flow is retarded by air diffusion; therefore vapor flux is larger than air flux. As the vapor flows inward the lower temperatures encountered cause condensation. Figure 17 summarizes in a more conventional plot the flow patterns depicted in Figures 15 and 16.

The evaporation-rate curve and the temperature curves shown in Figure 8 are interrelated. We have discussed the effect of surface evaporation on the temperature profiles vs. time. Now let us turn to the effect of surface temperature on the evaporation-rate curve. In mild heating conditions, surface evaporation is essentially governed by two factors, namely the surface temperature and the fraction of wet surface. In the beginning, fast increase of the evaporation rate is mainly due to the rapid increase of surface temperature, because liquid supply from the interior is sufficient to maintain the surface totally wet. As surface evaporation increases, it reaches a point where the rate of liquid supply to the surface becomes less than the rate of surface evaporation and the surface starts to dry off; therefore the increase of evaporation rate is slowed down. In the middle, when the surface is relatively dry and the temperature increase is substantially slowed due to a high evaporation rate, the evaporation curve passes a maximum. Although the temperature increase is slightly accelerated toward the end of the heating period, the fast decrease in wet surface forces the evaporation curve to decline.

ACKNOWLEDGMENT

Paper No. 13,493. Scientific Journal Series, Minnesota Agricultural Experiment Station, St. Paul, MN 55108. Projects 18-027 and 18-063.

NOTATION

A_{eff} = fraction of wet surface
C_{pi} = constant pressure heat capacity of phase i, J/kg·k
$D_{\text{eff},a}$ = total effective diffusivity tensor of air in air-water vapor mixture, m^2/s
g = gravity vector, m/s
h = heat transfer coefficient, W/m^2·K
Δh_{vap} = enthalpy of vaporization per unit mass, J/kg
K = permeability tensor, μm^2
k_ϵ = $-\partial P_c(\epsilon_l,T)/\partial\epsilon_l$, N/m^2
k_g = gas phase relative permeability
k_l = liquid phase relative permeability
k_T = $-\partial P_c(\epsilon_l,T)/\partial T$, N/m^2·K
k_x = mass transfer coefficient, mol/m^2·s
M = molecular weight, kg/mol
$\dot{m}$ = mass rate of evaporation per unit volume, kg/m^3·s
N_{as} = molar flux of air at surface, mol/m^2s
N_{vs} = molar flux of water vapor at surface, mol/m^2·s
n = unit outer normal vector to surface
P_{atm} = atmospheric pressure, N/m^2
P_c = capillary pressure, N/m^2
P_g = gas pressure, N/m^2
R = radius, cm
R_g = gas constant, J/mol·K
r = radial coordinates, cm
T_c = critical temperature of water, K
T_r = room temperature, K
T = temperature, K
t = time, s
U = liquid saturation or fraction of porespace filled with liquid, ϵ_l/ϕ
$V^{(1)}$ = dimensionless water vapor density
$V^{(2)}$ = dimensionless air density
V_l = molar volume of liquid water, m^3/mol
$\bar{v}$ = local superficial flow rate, m/s
W = convective air flow rate in oven, m/s
x = dimensionless radial coordinate
x_w = mole fraction of water vapor

Greek Letters

α = thermal diffusivity, m^2/s
ϵ = volume fraction
ϵ_c = percolation threshold
ϵ_l = volume fraction of phase i
θ = dimensionless temperature
κ = thermal conductivity
κ_{eff} = total thermal conductivity tensor, m^2/s
κ_i = thermal conductivity of phase i, W/m·K
μ = viscosity, kg/m·s
ρ = density, kg/m^3
ϕ = porosity
τ = dimensionless time
ω = angular velocity, rad/s

Subscripts

a = property of air
e = property of environment
g = property of gas
i = initial condition
l = property of liquid water
s = property of solid
r = room temperature
v = property of water vapor

APPENDIX

With the dimensionless variables defined in Eqs. 15–20, the thermal energy equation can be nondimensionalized as follows:

$$\frac{\partial\theta}{\partial\tau} - E_1\frac{\partial P_g}{\partial x}\frac{\partial\theta}{\partial x} + E_1\frac{\partial P_c}{\partial x}\frac{\partial\theta}{\partial x} - E_2\frac{\partial P_g}{\partial x}\frac{\partial\theta}{\partial x} + E_3 = E_4\frac{\partial U}{\partial x}\frac{\partial\theta}{\partial x} + E_5\frac{\partial^2\theta}{\partial x^2} + E_5\frac{1}{x}\frac{\partial\theta}{\partial x}. \quad \text{(A1)}$$

where

$$E_1 = \rho_l C_{pl} K_l/(\mu_l \cdot E_6)$$

$$E_2 = \{[V^{(1)}(\rho_{v_i} - \rho_{ve}) + \rho_{ve}]C_{pv} + V^{(2)}\rho_{ae}C_{pa}\}K_g/(\mu_g \cdot E_6)$$

$$E_3 = \Delta h_{\text{vap}}\dot{m}R^2/[(T_i - T_e)\cdot E_6]$$

$$E_4 = (\kappa_l - \kappa_g)\epsilon_{l_i}/E_6]$$

$$E_5 = (\epsilon_s\kappa_s + \epsilon_{l_i}U\kappa_l + \epsilon_g\kappa_g)/E_6$$

and

$$E_6 = \alpha_s\{\epsilon_s\rho_s C_{ps} + \epsilon_{l_i}U\rho_l C_{pl} + \epsilon_g[(V^{(1)}(\rho_{v_i} - \rho_{ve}) + \rho_{ve})C_{pv} + V^{(2)}\rho_{ae}C_{pa}]\}$$

ϵ_{l_i} denotes initial liquid volume fraction, and in this work $\epsilon_{l_i} = \phi$, the porosity.

The above equation can be discretized as follows:

$$\left\{-\frac{E^n_{1,i}(P^n_{g,i+1}-P^n_{g,i-1})}{4(\Delta x)^2} + \frac{E^n_{1,i}(P^n_{c,i+1}-P^n_{c,i-1})}{4(\Delta x)^2} - \frac{E^n_{2,i}(P^n_{g,i+1}-P^n_{g,i-1})}{4(\Delta x)^2} - \frac{E_{4,i}(U^n_{i+1}-U^n_{i-1})}{4(\Delta x)^2} + \frac{E^n_{5,i}}{(\Delta x)^2} - \frac{E^n_{5,i}}{2(i-1)(\Delta x)^2}\right\}\theta^{n+1}_{i-1} + \left\{-\frac{1}{\Delta\tau} - \frac{2E^n_{5,i}}{(\Delta x)^2}\right\}\theta^{n+1}_i + \left\{\frac{E^n_{1,i}(P^n_{g,i+1}-P^n_{g,i-1})}{4(\Delta x)^2} - \frac{E^n_{1,i}(P^n_{c,i+1}-P^n_{c,i-1})}{4(\Delta x)^2}\right.$$

$$+\frac{E^n_{2,i}(P^n_{g,i+1}-P^n_{g,i-1})}{4(\Delta x)^2}+\frac{E_{4,i}(U^n_{i+1}-U^n_{i-1})}{4(\Delta x)^2}+\frac{E^n_{5,i}}{(\Delta x)^2}+\frac{E^n_{5,i}}{2(i-1)(\Delta x)^2}\Bigg\}\theta^{n+1}_{i+1}=-\frac{\theta^n_i}{\Delta\tau}+E^n_{3,i} \quad \text{(A2)}$$

where subscripts $i-1$, i and $i+1$ indicate consecutive positions, and superscripts n and $n+1$ denote old and new time levels, respectively.

Similarly, the liquid phase continuity equation in dimensionless form becomes

$$\frac{1}{\rho_l}\frac{\partial(U\rho_l)}{\partial\tau}-F_1\frac{1}{x}\frac{\partial P_g}{\partial x}-F_2\frac{1}{x}\frac{\partial U}{\partial x}-F_3\frac{1}{x}\frac{\partial\theta}{\partial x}-F_4\frac{\partial K_l}{\partial x}\frac{\partial P_g}{\partial x}-F_1\frac{\partial^2 p_g}{\partial x^2}-F_5\frac{\partial(K_lk_\epsilon)}{\partial x}\frac{\partial U}{\partial x}-F_2\frac{\partial^2 U}{\partial x^2}-F_6\frac{\partial(k_lk_T)}{\partial x}\frac{\partial\theta}{\partial x}-F_3\frac{\partial^2\theta}{\partial x^2}+F_7=0 \quad \text{(A3)}$$

where

$$F_1=K_l/\mu_l\alpha_s\epsilon_{l_i}$$
$$F_2=K_lk_\epsilon/\mu_l\alpha_s$$
$$F_3=(T_i-T_e)K_lk_T/\mu_l\alpha_s\epsilon_{l_i}$$
$$F_4=1/\mu_l\alpha_s\epsilon_{l_i}$$
$$F_5=1/\mu_l\alpha_s$$
$$F_6=(T_i-T_e)/\mu_l\alpha_s\epsilon_{l_i}$$

and

$$F_7=\dot{m}R^2/\alpha_s\epsilon_{l_i}\rho_l$$

The above equation can be discretized as follows:

$$\Bigg\{-\frac{F^n_{2,1}}{2(i-1)(\Delta x)^2}-\frac{F^n_{5,i}(K^n_{l,i+1}k^n_{\epsilon,i+1}-K^n_{l,i-1}k^n_{\epsilon,i-1})}{4(\Delta x)^2}+\frac{F^n_{2,i}}{(\Delta x)^2}\Bigg\}U^{n+1}_{i-1}-\frac{2F^n_{2,i}}{(\Delta x)^2}U^{n+1}_i+\Bigg\{\frac{F^n_{2,i}}{2(i-1)(\Delta x)^2}+\frac{F^n_{5,i}(K^n_{l,i+1}k^n_{\epsilon,i+1}-K^n_{l,i-1}k^n_{\epsilon,i-1})}{4(\Delta x)^2}+\frac{F^n_{2,i}}{(\Delta x)^2}\Bigg\}U^{n+1}_{i+1}$$
$$=\frac{U^{n+1}_i\rho^{n+1}_{l,i}-U^n_i\rho^n_{l,i}}{\rho^n_{l,i}\Delta\tau}-\frac{F^n_{1,i}(P^n_{g,i+1}-P^n_{g,i-1})}{2(i-1)(\Delta x)^2}-\frac{F^n_{3,i}(\theta^n_{i+1}-\theta^n_{i-1})}{2(i-1)(\Delta x)^2}-\frac{F^n_{4,i}(K^n_{l,i+1}-K^n_{l,i-1})(P^n_{g,i+1}-P^n_{g,i-1})}{4(\Delta x)^2}$$
$$-\frac{F^n_{1,i}(P^n_{g,i+1}-2P^n_{g,i}+P^n_{g,i-1})}{(\Delta x)^2}-\frac{F^n_{6,i}(K^n_{l,i+1}k^n_{T,i+1}-K^n_{l,i-1}k^n_{T,i-1})(\theta^n_{i+1}-\theta^n_{i-1})}{4(\Delta x)^2}$$
$$-\frac{F^n_{3,i}(\theta^n_{i+1}-2\theta^n_i+\theta^n_{i-1})}{(\Delta x)^2}+F^n_{7,i} \quad \text{(A4)}$$

The gas phase diffusion equation has the following dimensionless form:

$$\frac{\partial\epsilon_gV^{(2)}}{\partial\tau}=G_1\frac{V^{(2)}}{x}\frac{\partial P_g}{\partial x}+G_2V^{(2)}\frac{\partial K_g}{\partial x}\frac{\partial P_g}{\partial x}+G_1\frac{\partial V^{(2)}}{\partial x}\frac{\partial P_g}{\partial x}+G_1V^{(2)}\frac{\partial^2P_g}{\partial x^2}+\frac{G_3}{x}\frac{\partial V^{(2)}}{\partial x}+G_5\frac{\partial D_{\text{eff2}}}{\partial x}\frac{\partial V^{(2)}}{\partial x}+G_3\frac{\partial^2V^{(2)}}{\partial x^2}-G_4V^{(2)}\frac{1}{x}\frac{\partial\rho_g}{\partial x}-G_5V^{(2)}\frac{\partial(D_{\text{eff2}}/\rho_g)\partial\rho_g}{\partial x}\frac{\partial\rho_g}{\partial x}-G_4\frac{\partial V^{(2)}}{\partial x}\frac{\partial\rho_g}{\partial x}-G_4V^{(2)}\frac{\partial^2\rho_g}{\partial x^2} \quad \text{(A5)}$$

where

$$G_1=K_g/\alpha_s\mu_g$$
$$G_2=1/\alpha_s\mu_g$$
$$G_3=D_{\text{eff2}}/\alpha_s$$
$$G_4=D_{\text{eff2}}/\alpha_s\rho_g$$

and

$$G_5=1/\alpha_s$$

Equation A5 can be approximated by the following finite difference form.

$$\Bigg\{-G^n_{1,i}\frac{(P^n_{g,i+1}-P^n_{g,i-1})}{4(\Delta x)^2}-\frac{G^n_{3,i}}{2(i-1)(\Delta x)^2}-\frac{G^n_{5,i}(D^n_{\text{eff2},i+1}-D^n_{\text{eff2},i-1})}{4(\Delta x)^2}+\frac{G^n_{3,i}}{(\Delta x)^2}+\frac{G^n_{4,i}(\rho^n_{g,i+1}-\rho^n_{g,i-1})}{4(\Delta x)^2}\Bigg\}V^{(2),n+1}_{i-1}$$
$$+\Bigg\{-\frac{\epsilon^{n+1}_{g,i}}{\Delta\tau}+\frac{G^n_{1,i}(P^n_{g,i+1}-P^n_{g,i-1})}{2(i-1)(\Delta x)^2}+\frac{G^n_{2,i}(K^n_{g,i+1}-K^n_{g,i-1})(P^n_{g,i+1}-P^n_{g,i-1})}{4(\Delta x)^2}+\frac{G^n_{1,i}(P^n_{g,i+1}-2P^n_{g,i}+P^n_{g,i-1})}{(\Delta x)^2}-\frac{2G^n_{3,i}}{(\Delta x)^2}-\frac{G^n_{4,i}(\rho^n_{g,i+1}-\rho^n_{g,i-1})}{2(i-1)(\Delta x)^2}$$
$$-\frac{G^n_{5,i}[(D^n_{\text{eff2}}/\rho_g)^n_{i+1}-(D_{\text{eff2}}/\rho_g)^n_{i-1}](\rho^n_{g,i+1}-\rho^n_{g,i-1})}{4(\Delta x)^2}-\frac{G^n_{4,i}(\rho^n_{g,i+1}-2\rho^n_{g,i}+\rho^n_{g,i-1})}{(\Delta x)^2}\Bigg\}V^{(2),n+1}_i$$
$$+\Bigg\{\frac{G^n_{1,i}(P^n_{g,i+1}-P^n_{g,i-1})}{4(\Delta x)^2}+\frac{G^n_{3,i}}{2(i-1)(\Delta x)^2}+\frac{G^n_{5,i}(D^n_{\text{eff2},i+1}-D^n_{\text{eff2},i-1})}{4(\Delta x)^2}+\frac{G^n_{3,i}}{(\Delta x)^2}-\frac{G^n_{4,i}(\rho^n_{g,i+1}-\rho^n_{g,i-1})}{4(\Delta x)^2}\Bigg\}V^{(2),n+1}_{i+1}=\frac{\epsilon^n_{g,i}V^{(2),n}_i}{\Delta\tau} \quad \text{(A6)}$$

The gas phase diffusion equation was discretized as follows to calculate $\dot{m}$.

$$\frac{\alpha_s}{R^2}\frac{(\epsilon^{n+1}_{g,i}\rho^{n+1}_{g,i}-\epsilon^n_{g,i}\rho^n_{g,i})}{\Delta\tau}-\frac{\rho^{n+1}_{g,i}K^{n+1}_{g,i}}{\mu_gR^2(i-1)\Delta x}\frac{(P^{n+1}_{g,i+1}-P^{n+1}_{g,i-1})}{2\Delta x}-\frac{(\rho^{n+1}_{g,i+1}K^{n+1}_{g,i+1}-\rho^{n+1}_{g,i-1}K^{n+1}_{g,i-1})}{\mu_gR^2(2\Delta x)}\frac{(P^{n+1}_{g,i+1}-P^{n+1}_{g,i-1})}{2\Delta x}-\frac{\rho^{n+1}_{g,i}K^{n+1}_{g,i}}{\mu_g}\frac{P^{n+1}_{g,i+1}-2P^{n+1}_{g,i}+P^{n+1}_{g,i-1}}{R^2(\Delta x)^2}=\dot{m}^{n+1}_i \quad \text{(A7)}$$

LITERATURE CITED

ASME Steam Tables, ASME (1967).

Bird, R. B., W. E. Stewart, and E. N. Lightfoot, *Transport Phenomena*, John Wiley, New York (1960).

Ceaglske, N. H., and O. A. Hougen, "Drying Granular Solids," *Ind. Eng. Chem* **29**, 805 (1937).

Collins, R. E., *Flow of Fluids Through Porous Materials*, Litton Educ. Pub., New York (1961).

Gurr, C. G., T. J. Marshall, and J. T. Hutton, "Movement of Water in Soil Due to a Temperature Gradient," *Soil Sci.*, **74**, 335 (1952).
Harmathy, T. Z., "Simultaneous Moisture and Heat Transfer in Porous Systems with Particular Reference to Drying," *I & EC Fund.*, **8**(1), 92 (1969).
Heiba, A. A., et al., "Percolation Theory of Two-Phase Relative Permeability," *SPE Reprint* No. 11,015 (Sept., 1982).
Hoffman, R. N., "A Technique for the Determination of Capillary Pressure Curves Using a Constantly Accelerated Centrifuge," *Trans. AIME*, **228**, 227 (Sept., 1963).
Huang, C. L. D., H. H. Sinag, and C. H. Best, "Heat and Moisture Transfer in Concrete Slabs," *Int. J. Heat and Mass Transfer*, **22**, 257 (1979).
Hung, C. C., "Water Migration and Structural Transformation of Oven Cooked Meat," Ph.D. Thesis, Univ. of Minnesota (1980).
Jefferson, T. B., O. W. Witzell, and W. L. Sibit, "Thermal Conductivity of Graphite-Silicone Oil and Graphite-Water Suspensions," *Ind. Eng. Chem.*, **50**, 1,589 (1958).
Kirkpatrick, S., "Percolation and Conduction," *Rev. Mod. Phys.*, **45**, 574 (1973).
Larson, R. G., L. E. Scriven, and H. T. Davis, "Percolation Theory of Two-Phase Flow in Porous Media," *Chem. Eng. Sci.*, **36**, 57 (1981).
Lykov, A. V., and Y. A. Mykhaylov, *Theory of Energy and Mass Transfer*, Prentice-Hall, Englewood Cliffs, NJ (1961).
Mohanty, K. K., J. Ottino, and H. T. Davis, "Reaction and Transport in Disordered Composite Media: Introduction of Percolation Concepts," *Chem. Eng. Sci.*, **37**, 905 (1982).
Morse, R. A., P. L. Terwilliger, and S. T. Yuster, "Relative Permeability Measurements on Small Core Samples," *Oil and Gas J.*, **46**, 109 (1947).
Myers, G. E., *Analytical Methods in Conduction Heat Transfer*, McGraw-Hill, (1971).
Pathak, P., "Porous Media: Structure, Strength, and Transport," Ph.D. Thesis, Univ. of Minnesota (1981).
Peck, R. E., K. C. Vyas, and R. Toei, "Capillary Theory Applied to Drying," *AIChE Symp. Ser.*, No. 163, **73**, 63 (1977).
Perry, R. H., and C. H. Chilton, Eds., *Chemical Engineer's Handbook*, 5th ed., McGraw-Hill, New York (1973).
Scheidegger, A. E., *The Physics of Flow-Through Porous Media*, 3rd ed., Univ. of Toronto Press (1972).
Sherwood, T. K., "Application of the Theoretical Diffusion Equations to the Drying of Solids," *Trans. AIChE*, **27**, 190 (1931).
Toei, R., and M. Okazaki, "The Drying Mechanism of Capillary-Porous Materials," *Inzh. Fiz. Zh.*, **19**(3), 464 (1970).
Villadsen, J. V., and W. E. Stewart, "Solution of Boundary Value Problems by Orthogonal Collocation," *Chem. Eng. Sci.*, **22**, 1,483 (1967); **23**, 1,515 (1968).
Weast, R. C., and M. J. Astle, Eds., *CRC Handbook of Chemistry and Physics*, 63rd ed. (1982).
Wei, C. K., et al., "Water Loss and Shrink in Hybrid-Oven Cooked Meat," *Int'l. Inst. of Microwave Power Symp.*, Edmonton, Alb., Canada, 184 (1981).
Whitaker, S., "Simultaneous Heat, Mass and Momentum Transfer in Porous Media: A Theory of Drying," *Advances in Heat Transfer*, **13**, 119 (1977).

Manuscript received May 23, 1983, revision received Oct. 18, and accepted Oct. 20, 1983.